Insight into rotational effects on a horizontal axis wind turbine NREL phase II using CFD simulation and inverse BEM

Riyadh Belamadi[1], Mdouki Ramzi[2], Adrian Ilinca[3], Djemili Abdelouaheb[1]

[1]*Mechanical of Materials and Industrial Maintenance Laboratory LR3MI, University of Annaba, ALGERIA*
[2]*Energy and Turbomachinery Laboratory, Mechanical Department, University of Tébessa, ALGERIA*
[3]*Wind Energy Research Laboratory, University of Québec at Rimouski 300, Québec, CANADA*
Belaamdi.Riyadh@gmail.com

Abstract – *The present work aims to study the aerodynamic characteristics of the NREL phase II rotor (generated only with S809 profile along the span for an untwisted case) that is a horizontal axis downwind wind turbine rotor and which is assumed to stand isolated in the space. The three-dimensional steady-incompressible flow Reynolds Averaged Navier-Stokes equations are solved by using the commercial CFD package ANSYS FLUENT and, the turbulence closure model k-ω with shear stress transport correction was adopted for all computations. The computations were done for wind speed of 7.2, 10.56, 12.85, 16.3, and 9.18 m.s⁻¹. Results of pressure and torque for considered wind turbine rotor have been directly compared to the available experimental data. The comparisons show that CFD results along with the turbulence model can predict the span-wise loading of the wind turbine rotor with reasonable agreement. Secondly, A comparison of lift and drag coefficients was made between the results obtained using the inverse algorithm BEM based on the calculated pressure distributions and the experimental test data. The result show that the general trend is similar for all sections of the scale, however, large deviation exists between the 2-D and 3-D case.*

Keywords:*CFD computation, RANS, Horizontal axis wind turbine, inverse BEM, Rotational effect, turbulent flow.*

I. Introduction

Wind energy is becoming a significant contributor to the world's electrical energy generation systems and it is the fastest growing source of energy in the world today. Numerical solution of flows through wind turbines is increasingly useful since it helps reduce time and costs in wind turbine development. The literature reports various methods that compare numerical predictions to experiments. The Blade-Element momentum Method [1] consists of dividing the flow in annular control volumes and applying momentum balance and energy conservation in each control volume. The method is indeed computationally cheap and thus very fast, providing very satisfactory results [2]. In the Actuator Disc Method, the rotor is represented by a permeable disc that allows the flow to pass through it. The classical actuator disc model is based on conservation of mass, momentum and energy, and constitutes the main ingredient in the 1-D momentum theory, as originally formulated by Rankine and Froude [3]. Vortex lattice [4], lifting line, panel and vortex methods are also used to predict and design wind turbine rotors [5]. This list is far to be exhaustive.

The first applications of CFD to wings and rotor configurations were studied back in the late seventies and early eighties, in connection with aircraft wings and helicopter rotors, using potential flow solvers. In the field of aerodynamic research this technique has become increasingly important and it is prominent for studying turbo machinery. Natalino et al [6] used the RANS (Reynolds Averaged Navier-Stokes) equations to solve the 3-D turbulent-steady incompressible flow of HAWT, the results show that the predicted values of the power generated are in good agreement with those calculated with BEM method using the Spalart-Allmaras and the k-ω SST turbulence models for closure. Le Pape and Lecanu [7] performed several 2-D and 3-D Navier-Stokes computations with the compressible elsA solver and compared with test results by NREL in the NASA Ames large wind tunnel. The results of 2-D computation show that the k-ω with the addition of SST correction gives the best results. Indeed the SST correction allows to detect the stall angle of the airfoil. According to the same authors, for the 3-D computation, the comparison of the torque with experiments shows good agreement at low wind speeds but important differences at high speeds. RANS solver was also used for prediction of aerodynamic loads on NREL Phase II, III and VI, the result showed good agreement with experimental results [8, 9].

Wind turbine blades are strongly affected by the effects of rotation and 3-D flow and they often operate under stall conditions. However, the actual design approach is generally based on the use of the theory of

the blade element (BEM), with the lift and drag forces determined from measurements in 2-D. The results obtained are reasonably accurate in the vicinity of the design point, but in stalled conditions, BEM is known to under predict the forces acting on the blades [10]. In addition, the accurate prediction of the aerodynamic load of the rotor, even in stalled conditions, is of great importance for the dimensioning of the generator and other mechanical components.

In 1945 Himmelskamp [11] described by measurements the 3-D and rotational effects on the boundary layer of a propeller, where he found that the lift coefficient is higher when moving towards the axis of rotation. Later, other experimental studies have confirmed these initial results. Measurements were performed on wind turbine blades by Ronsten [12], showing the differences between the pressure coefficient of a rotating and non-rotating blades. Tangler and Kocurek [13] combine the results of measurements with classical BEM method to correctly compute lift and drag coefficients and the rotor power under stall conditions.

The theoretical foundations of the analysis of the rotation effects of rotating blades come thereafter, with Sears [14] who derived a set of equations for the potential flow field around a cylindrical blade infinite range in pure rotation. He said that the radial component (spanwise) of the speed depends only on the potential flow and is independent of the span. Then Fogarty and Sears [15] extended the first study on the potential flow around a rotating blade. They confirmed that the tangential and axial velocity components are the same as in the case of 2-D at the local relative speed and the local angle of attack. A more complete work was done by Fogarty [16], which consists of the numerical calculations of the laminar boundary layer of a hub and a blade with a thickness. It is shown that the line of separation of the boundary layer is not affected by the rotation, the spanwise velocity in the boundary layer appeared small compared to the chordwise direction, and no large effect of the rotation was observed, contrary to what has been described in the work of Himmelskamp [11]. A theoretical analysis was made by Banks and Gadd [17], focused on demonstrating how the rotation delays the separation of the laminar boundary layer. They found that the point of separation is delayed due to the rotation. The so-called secondary effects in the laminar incompressible boundary layer propeller and the rotor helicopters are extensively studied in the NASA report by McCroskey and Dwyer [18] by means of a combined numerical and analytical approach. They showed that approaching the axis of rotation, the Coriolis force in the cross flow direction becomes more important. On the other hand, the centrifugal pumping effect is much lower than it was supposed before, but its contribution increases when the magnitude of the adverse pressure gradient increases.

In the last decades, many studies were done on the rotating boundary layer using the computational fluid dynamics CFD. Sorenson [19] numerically solved the 3-D equations of the boundary layer on a rotating surface, using a viscous-inviscid interaction model. Snel et al. [10] are introducing a quasi-3D approach, based on viscous-inviscid interaction approach and compared with measurement. Du and Selig [20] approached the problem by solving the 3-D incompressible steady boundary layer equations. Also, a study of stall delay for wind turbines was done by Hu et al. [21] using the full N-S computations, wind tunnel measurement and boundary layer analysis.

The airfoil characteristics used in BEM codes are mostly based on 2D wind tunnel measurements of airfoils with constant span. However, a BEM code using airfoil data obtained directly from 2D wind tunnel measurements will not yield the correct loading and power. Owing to the 3D nature of the flow over wind turbine blades, the measured airfoil characteristics will be different from the real characteristics. The flow will be altered partly due to the 3D properties of the blade geometry, which is most pronounced at the thick root section and near the blade tip, and partly because of rotational effects in the boundary layer. As a consequence, 2D airfoil characteristics have to be corrected before they can be used in a BEM code. For this purpose, the work presented here aims at giving a better understanding of the main influence of the rotational effect on the boundary layer and the determination of the effective angle of attack based on the numerical investigation of a three-bladed small-sized rotor from the Viscous and Aeroelastic Effects on Wind Turbine Blades - Phase II project [22]. The flow model is three-dimensional, at steady state, incompressible regime and the flow field is always assumed to be fully turbulent.

II. Numerical Procedure

II.1. Turbine Geometry

The experimental data for NREL Phase II is obtained from the IEA Annex XIV database [22]. This database was built as a contribution of many European research labs and the NREL to store and document the experimental data for various tested wind turbines and make it available to researchers. NREL phase-II rotor mounted on a downwind machine is a small three bladed HAWT rotor with 5.029 m radius [23], as shown in figure 1. The blades of the phase-II rotor are non-twisted and non-tapered with a constant cord of 0.4572 m. The NREL S809 airfoil (figure 2) series is used, except for the root. At 14.4% span the airfoil thickness is t/c=43% and decreases linearly to t/c=20.95% at 30% span, while outboard of 30%, thickness is constant at that value. The nominal rotation speed is 71.68 rpm and the pitch is 12 degree.

Table 1. NREL Phase II blade description

|	
Number of blades	3
Rotor diameter	10.06 m
RPM	72 tour/min
Rotor location	Downwind
Root extension	0.723 m
Pitch angle	12°
Blade profile	S809
Blade chord length	0.4572 m, constant along the span
Twist angle	0°
Blade thickness	At 14.4% span, t/c = 43% At 30% span, t/c = 21% Outward 30%span, t/c = 21%

Figure 1.NREL Phase II Roto.

Figure.1 NREL Phase II Roto

Figure 2.NREL S809 airfoil geometry

II.2. Computational Domain and Grid

At the initial stages of the project, efforts were focused on trying to create and compare different mesh cells and types; structured, unstructured, C-type and H-type. Due to its advantage, it was decided to use a structured H-type mesh, therefore increasing the grid generation times.

It also has to be noted that although the rotor is featured with three blades, only one blade is actually being treated by exploiting the 120 degrees periodicity of the three-bladed rotor (figure 3). The wind turbine tower and the ground effect were neglected; the computational domain is enclosed between a small inner cylinder where Euler-slip wall boundary condition was imposed and an outer cylinder with a symmetry boundary condition, the length of the radius of the domain equal to 3 times the rotor diameter (R) to eliminate far field effects. The inlet was placed at 2R upstream of the blade where a uniform wind speed was assumed as velocity inlet boundary condition. Turbulence conditions also have to be defined here with the fixed value of turbulent intensity and viscosity ratio. Pressure outlet boundary condition was applied at 10R on the downstream direction of the rotor and sets the pressure at the boundary at a specific static pressure value. In this study, the obvious choice was to put the value equal to zero so that the pressure at the outlet would be equal to the atmospheric operating pressure.

As shown in Figure 4, the solution has been done for only one third of the domain, includes one blade, and uses periodic boundary condition in order to account for all three blades with full domain. A hexahedral mesh of approximately 3.5 million cells (255x168x75 in x, y and z respectively) was generated. The thickness of the first cell to the wall was kept at 0.00002 m (Figure 5.c) so that the y+ value falls between 1 and 5 which is suitable for k-ω with SST correction model.
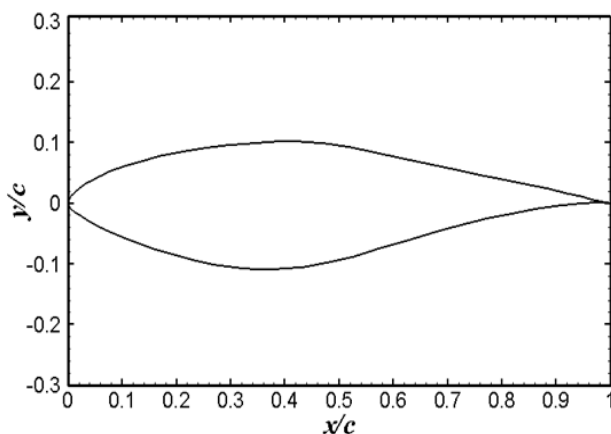
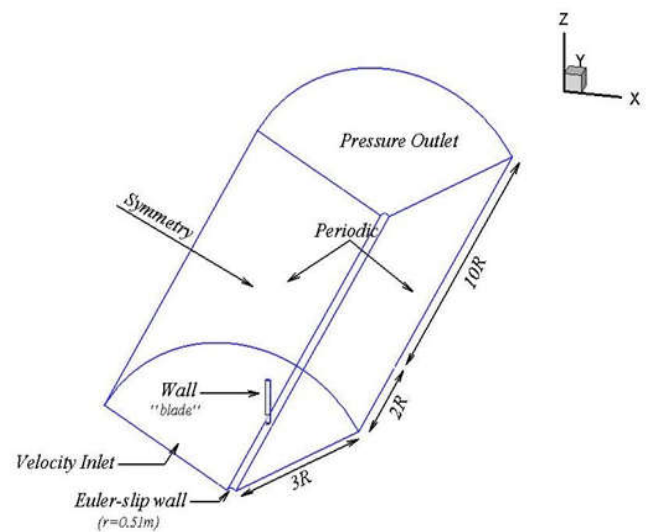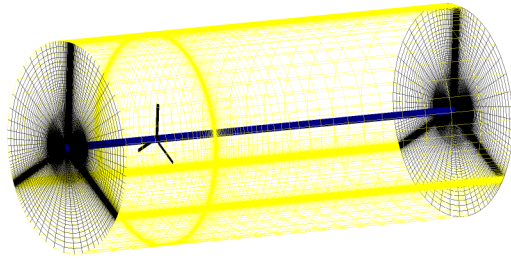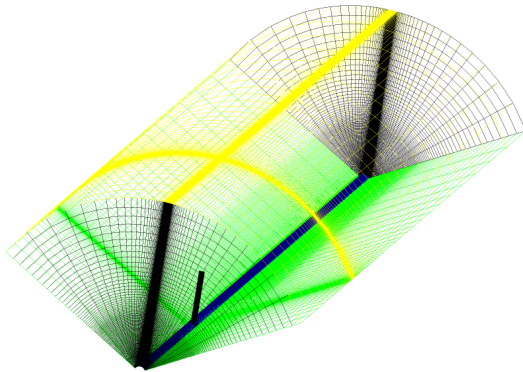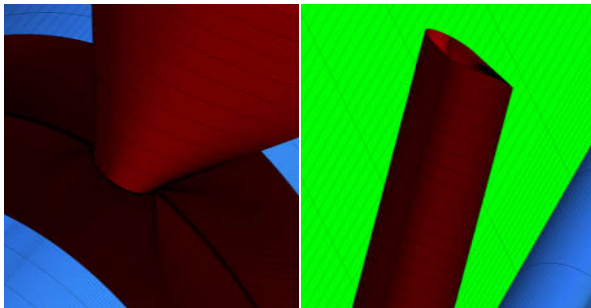
Figure 3.One Third-Cylindrical Domain and Boundary Condition.

(a)   All domain (360°).
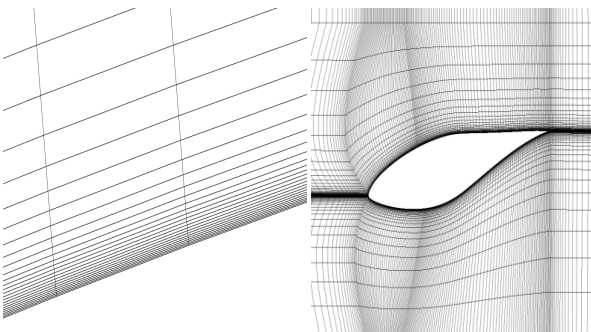

(a)   Periodicity application (120°).
Figure 4.Structured Mesh of the Domain.

(a)   Blade root.   (b)   Blade tip

(c)   Wall modeling approach   (d)   Surface mesh

Figure 5. 3-D Mesh for NREL Phase II.

II.3.   Solution Method

The equations of the fluid flow are usually solved by Fluent in a stationary reference frame. However, there are many problems that require the equations be solved in a moving reference frame. A rotating rotor of a wind turbine is such case. The one used here is called single moving reference frame (SRF). This latter permits an unsteady problem respect to the absolute reference frame to become steady in respect to the moving reference frame (Figure 6). In simple words, the whole computational domain is assumed to be rotating at the angular velocity of the turbine rotor [24]. This particular method is well suited for this problem since there is only one rotating wall.

The fluid velocities can be transformed from a stationary frame to a rotating frame in respect with flowing equations:

$$\vec{v}_r = \vec{v} - \vec{u}_r \qquad (1)$$

Where

$$\vec{u}_r = \vec{\omega} \times \vec{r} \qquad (2)$$

Where, $\vec{v}_r$ is the relative velocity (viewed from a rotating frame), $\vec{v}$ is the absolute velocity (viewed from a stationary frame), and $\vec{u}_r$ is the whirl velocity due to the rotating coordinate system.
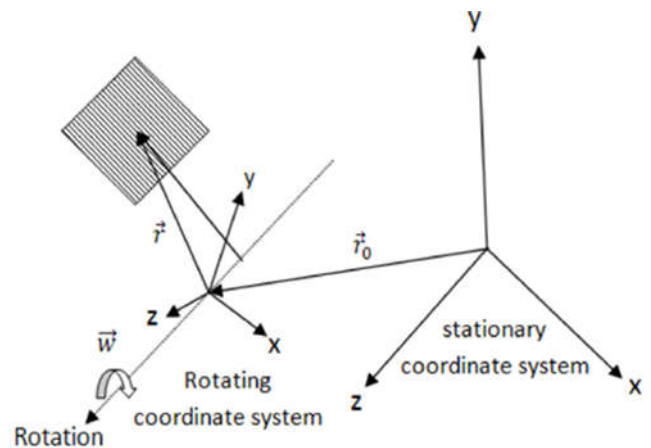

Figure 6.Rotating Reference Frames in view of stationary reference Frames [24].

The pressure-based discretization scheme is being applied with coupled algorithms, which solve in one step the system of momentum and pressure-based continuity equation. The solution was initialized with first-order upwind discretization scheme for all variables; pressure, momentum and turbulence equations, when some convergence is achieved, it can switch to second order. This is done in order to limit convergence problems. The number of iterations adjusted to reduce the scaled residual below the value of 10-5 which is the criterion of convergence. For each run, the observations of the static pressure, lift and drag coefficient were appointed for the convergence of the solution.

In previous work [25], 2-D computations are first

performed on the "classical" S809 airfoil in order to validate the computational setup and define the most suitable turbulence model among four possible choices (standard k–ε, Spalart–Allmaras, k–ω and k–ω SST). Based on comparison with experimental data, the computational results show that all the chosen turbulent models demonstrated good accuracy for solving the flow.

The k-ω turbulence model with SST correction has been used for all steady state CFD simulations.

III. Results

III.1. Pressure distribution

The quantity and type of results that can be extracted from this type of numerical study is large, starting from integral aerodynamics, to pressure distribution and up to wake study. Provided the aim of this study, results will restrict to pressure distribution on the blade, lift and drag coefficient, generated torque and a general overview of the flow field around the rotor. The numerical pressure distribution is presented and compared with experimental results at 30, 47, 63 and 80% spanwise locations for wind speed 7.2, 12.9 and 19.18m.s^{-1}.

At 7.2 m.s^{-1}, the computed pressure distribution at all sections of the blade is in good agreement with the experimental data (figure 7). At this wind speed, the flow is completely attached and no separation occurs except up to 30% span, where flow is separated on 30% chord length and we observe some deviation that is due to a known difficulty of RANS turbulence models in solving separated flow.

At 12.85 m.s^{-1}, important discrepancies between the computed and experimental pressure distribution on the suction side are observed in the r/R=0.30 section near the blade root (figure 8). Disagreement seems to increase with wind speed and especially for the suction side of the blade; at this speed stronger vortices were formed close to the root which explains such discrepancy.

At 19.18 m.s^{-1}, again there are differences at r/R= 0.3 on the suction side. At r/R=0.8 we observe a disagreement with the experimental result near the leading edge on the suction side as shown in figure 9. At this speed, due to the stronger vortices formed at the root and the tip of the blade it is very difficult to capture the separation characteristic using RANS turbulence models.

III.2. Flow Visualization

Since the relative velocity magnitude gives a more information for airfoil aerodynamics, the separation is investigated by plotting the streamlines and contour of relative velocity magnitude at different spanwise blade sections. The plots were obtained for wind speeds of 7.2, 12.85 and 19.18 m.s-1.

In (figure 10) can be observed that at 7.2 m.s-1 the flow is attached on most of the blade surface except for small regions at r/R= 0.3. The results obtained support the previous discussion (figure 7), where the pressure distribution in good agreement with experimental results.

At 12.85 m.s-1, the results give more precise information Figures 10; it can be observed that the separation with tow vortices occurs at r/R=0.3 on the suction side. The number of vortices decreases to one vortex at r/R=0.47 and vanishes at r/R=0.63 and r/R= 0.8. Again, the results support the previous discussion (figure 8). The discrepancy in pressure distribution also decreases as one goes from root to tip.

At 19.18 m.s-1, the separation effects are magnified at all blade sections (Figure 10), this explains the deviation of computed pressure distribution from experimental results for these sections (figure 9).

To give more precise information, the development of the limiting streamlines with static pressure contour for both blade sides is shown in Figure 11. At 7.2 m.s^{-1} can be observed that on the suction side the separation starts from the root to r/R=30%, due to the strong 3-D effects. At 12.85 m.s^{-1} separation seems to be widely experienced at r/R=80 % of the blade, while the separation occupies most of the suction side at 19.18 m.s^{-1} except for a small area near to the blade tip. On a rotating blade there are two main forces play an important role in separated boundary layer, i.e. the centrifugal forces that produce a spanwise pumping effect that leads to the deviation of the streamlines in spanwise direction towards the tip. On the other hand, Coriolis force, which acts in the chordwise direction as a favourable pressure gradient that tends to delay separation.
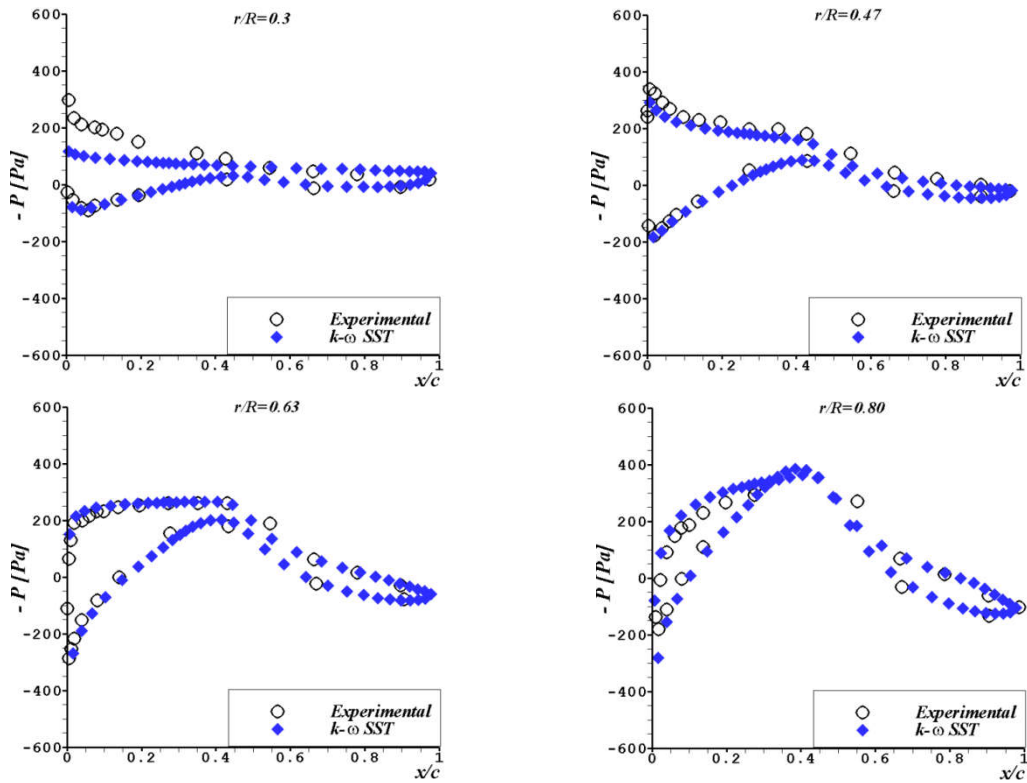
Figure 7.Pressure distribution comparison between experimental and calculated at different spanwise sections at 7.2 m.s^{-1} for NREL II.
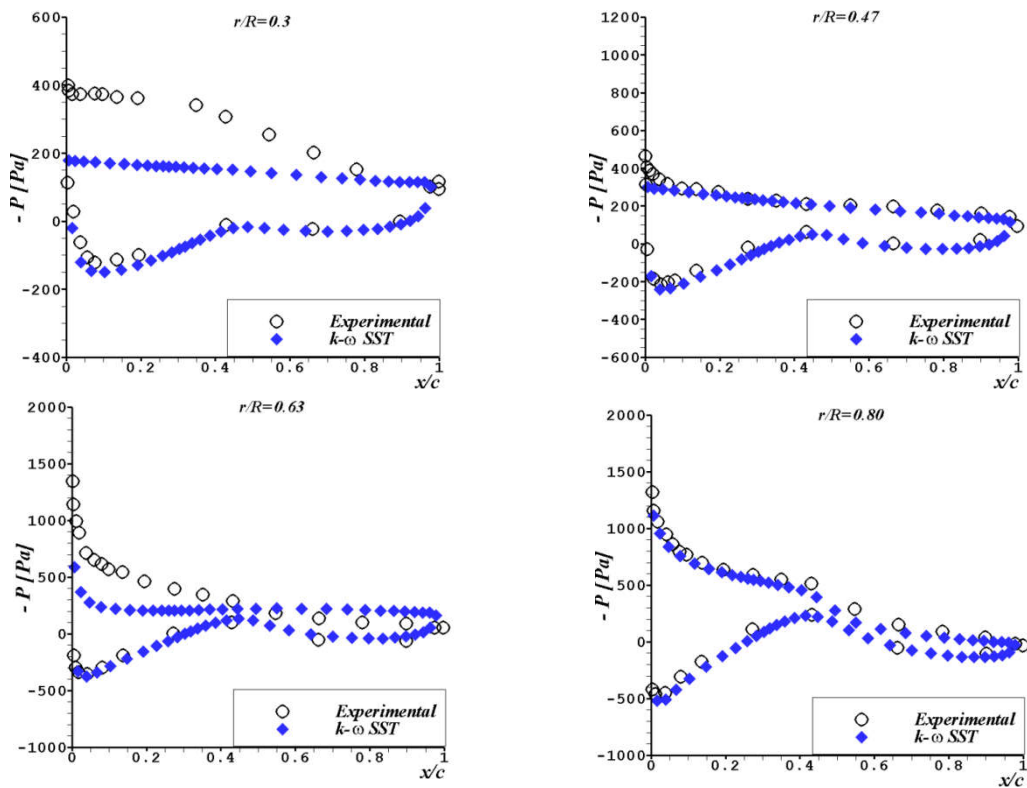

Figure 8.Pressure distribution comparison between experimental and calculated at different spanwise sections at 12.83 m.s^{-1} for NREL II.
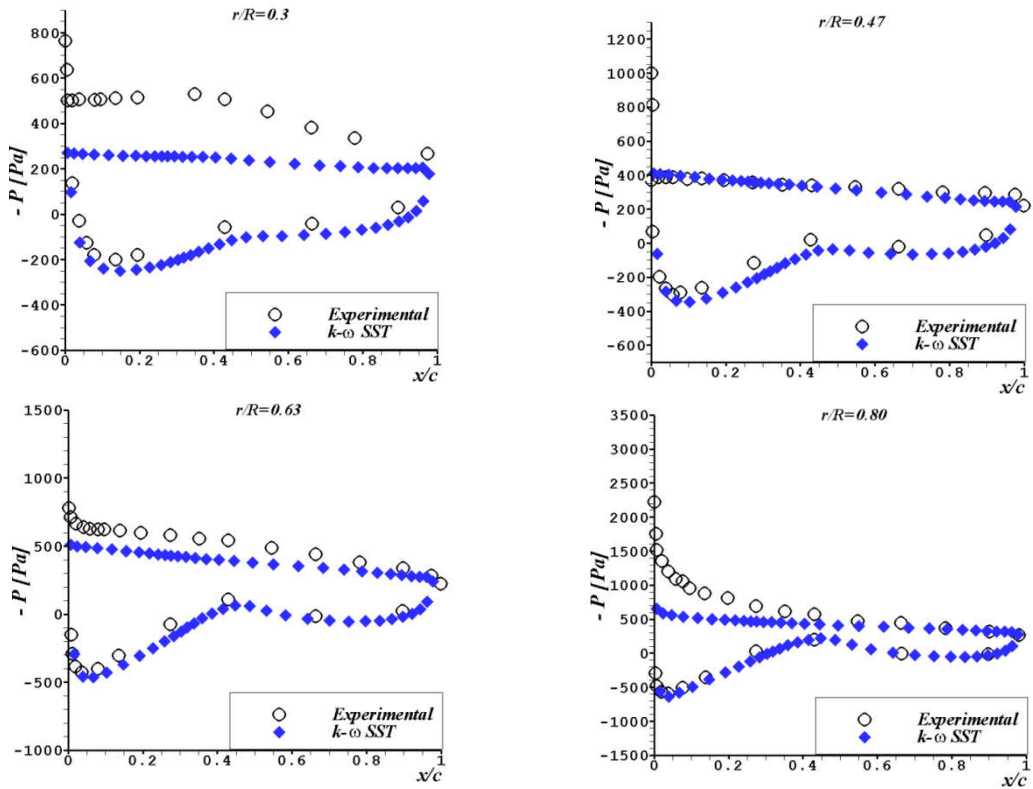
Figure 9.Pressure distribution comparison between experimental and calculated at different spanwise sections at 19.18 m.s^{-1} for NREL II.
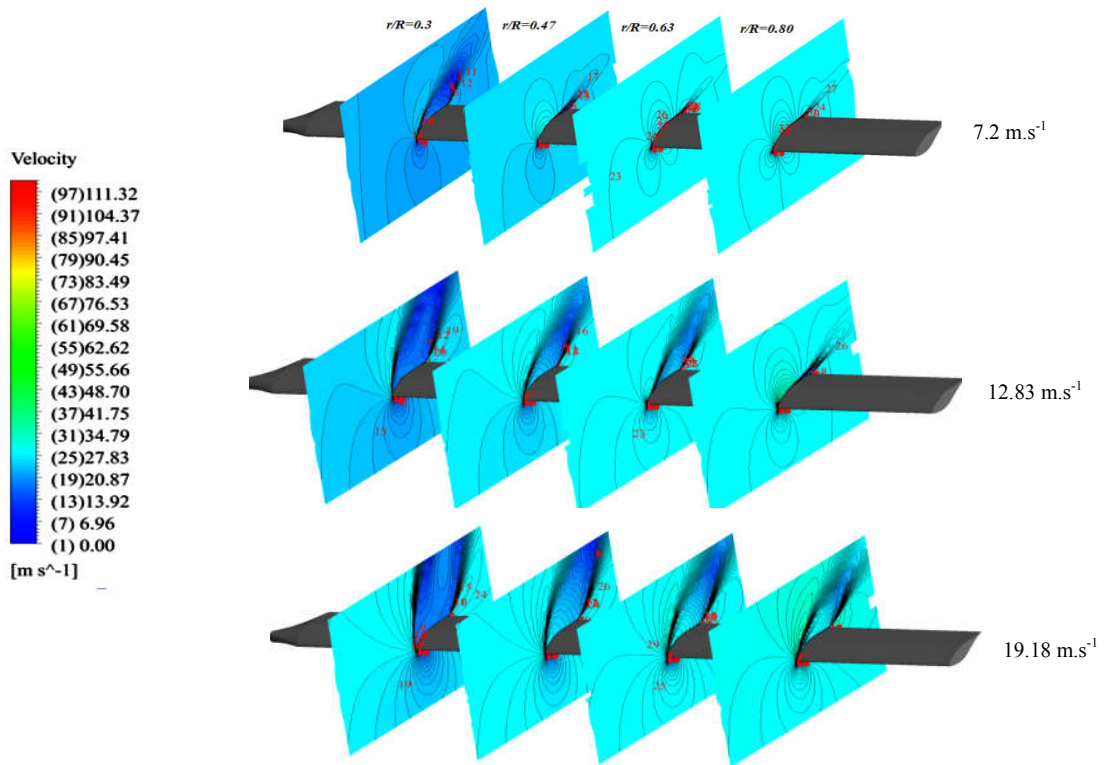

Figure 10.Relative velocity contours for all radial stations for different wind speeds.
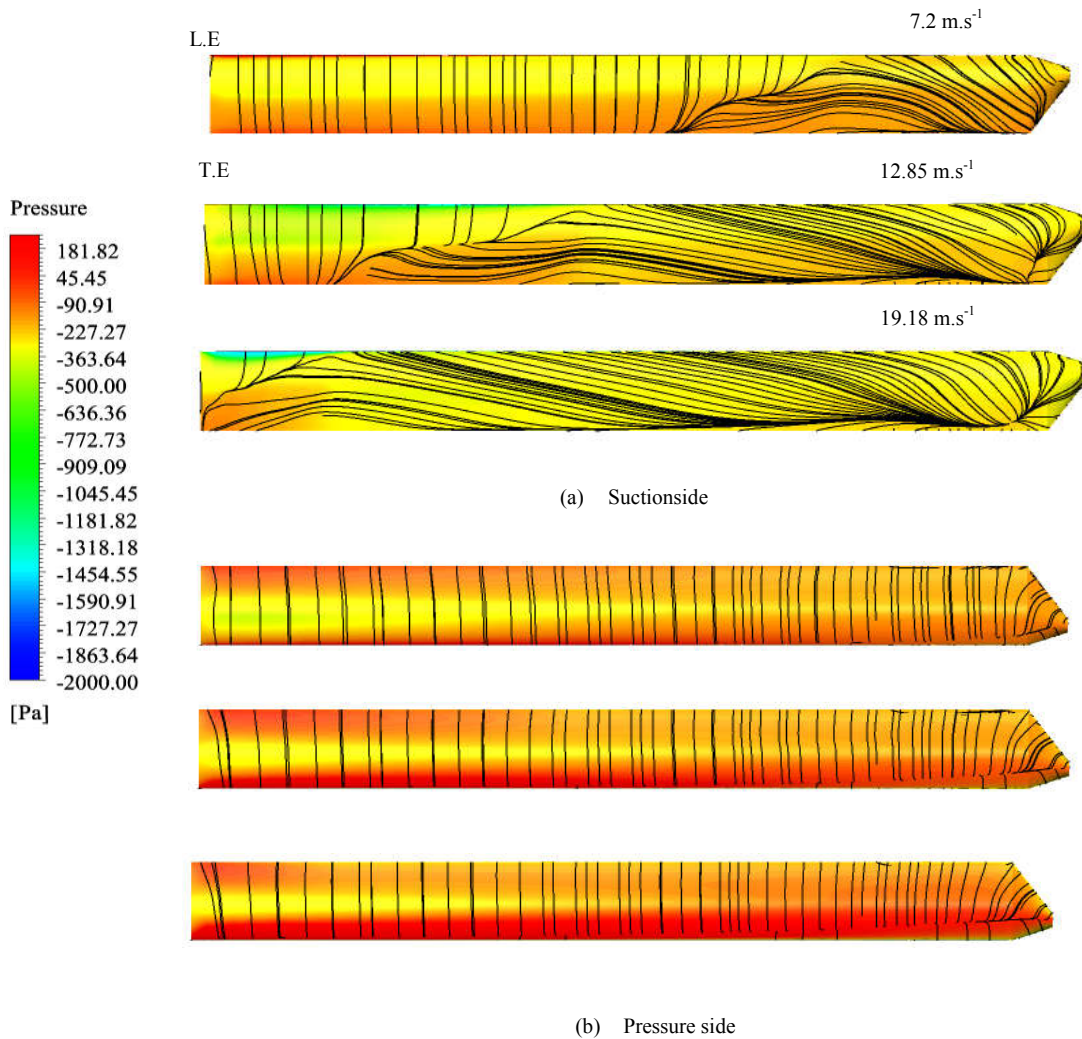
(a)   Suctionside

(b)   Pressure side

Figure 11. Limiting streamlines with static Pressure contour of NREL Phase II rotor at different wind speeds.

III.3.   Performance

The comparisons for the rotor torque are shown in Table 2. At 7.2 m.s^{-1} the computed torque has a better agreement with strain gages measurement than with the generator measurement; while at 10.56 m.s^{-1} the trend is reversed. This is perhaps due to the fact that at low wind speeds the blade flapping is low, thus the strain gage measurement is accurate while the generator correlation is not accurate in this region because it is far from its design operating condition [26]. With increasing speed, the blade flapping strengthens while the generator gets closer to its design operating range, hence the reverse behavior.

Table 2.Torque prediction errors at wind speeds 7.2 and 10.56 m.s-1 for

Wind speed [m.s^{-1}]	CFD	Experiment				
		Strain gage		Generator		
	Torque [Nm]	Torque [Nm]	Error [%]	Torque [Nm]	Error [%]	
7.2	290.51	286.22	1.49	317.26	-8.43	
10.56	1088.56	1207.39	-9.84	1190.04	-8.52	

NREL II..

In comparing the rotor torque derived power against the generator power, it was found that the efficiency did not match the published efficiency. As a result, a better curve fit between mechanical and generator power was found in [27], as described below:

$$P_{Generator} = 0.9036\, P_{Mechanical} - 0.847 \qquad (3)$$

The computed power as a function of the wind speed is shown in Figure 12 against the experimental IEA data [22], numerical results of Aerodyn/Yawdyn by Duque et al. [27] and BEM results by Ceyhan et al. [28]. For the computed power results, the mechanical power was corrected to generator power using equation (3). The CFD results are found to be in good agreement with those obtained using the BEM method and measured one, for the tested undisturbed wind speed, ranging from 7.2 to 12.83 m.s^{-1} for generally attached flow conditions.
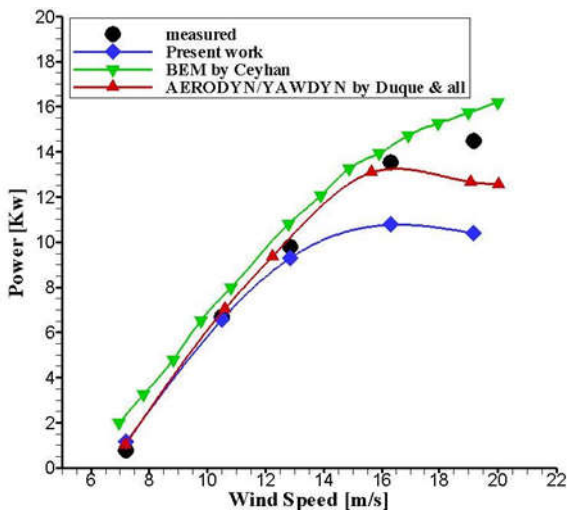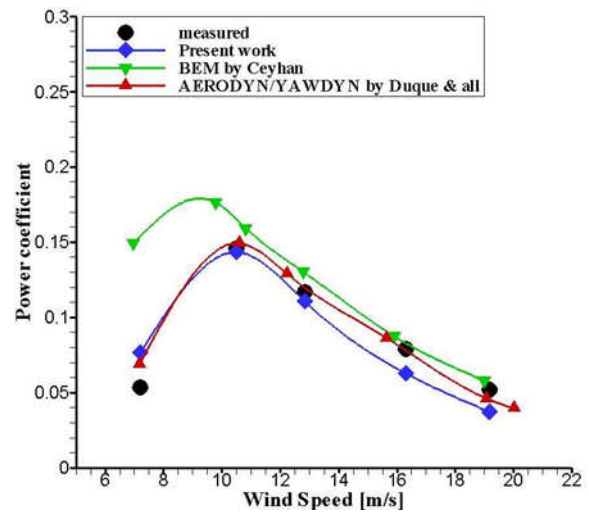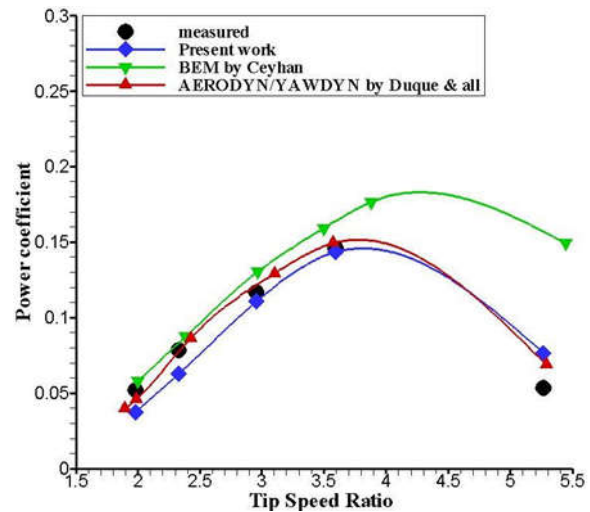

Figure.12. Variation of experimental (NREL Phase II) and computational power output as function of wind speed.

Figure 12 shows a comparison of the measured and computed power for various wind speeds and tip speed ratio. It is interesting to note that the CFD computations performed with Fluent have a similar trend with measured one and the other numerical results. In general, the numerical results for wind speed of 7.2 to 12.85 m.s^{-1} are in good agreement with those obtained using the BEM method and those measured. In fact, at 10.56 m.s^{-1} the calculated power value is less than that measured by 1.80%, and gradually as the wind speed increases the error of the calculated power increases. At 12.85, 16.3 and 19.18 m.s^{-1} the calculated power is lower than that measured by 5.22, 20.36 and 28.19% respectively. The results show differences at higher wind speeds as expected, considering the inability of the RANS model to accurately predict the aerodynamic loads in deep stall conditions.

Figure 13 shows a comparison of measured and calculated power coefficients for different wind speeds values and tip speed ratio respectively. It is interesting to note that the numerical solution has a similar trend with measures and with other numerical results. Note that the maximum value of the calculated power coefficient is only about 0.15, achieved at the speed of 10.56 m.s^{-1} and tip speed ratio 3.59. The value is well below the Betz limit (59.3%) and the maximum of modern wind turbines recently commercialized of approximately 45% [29]. At high wind speeds, the flow separation plays a major role in reducing the overall aerodynamic efficiency.

(a)

(b)

Figure.13. (a)Variation of experimental (NREL Phase II) and computational coefficient as function of wind speed. (b) Variation of experimental (NREL Phase II) and computational coefficient as function of tip speed ration.

III.4. Determination of the Effective Angle of Attack

The effects of rotation could be studied and identified, by comparing the 3-D calculations of the rotating blade with the corresponding 2-D situations. Nevertheless, the flow conditions in both cases must be carefully chosen, i.e. in a consistent manner. It is well known that the flow properties have similarities if the Reynolds number is kept the same [3], but in the wing sections theory the angle of attack is of equal importance. The angle of attack is a 2-D concept. It is defined as the geometric angle between the direction of the relative flow and the chord of theairfoil. Therefore, finding an equivalent angle of attack for the local 3-D flow is not trivial. For a rotary blade, further complication arises from the 3-D effects at the root and the tip of the blade.

Inverse blade element momentum method

The inverse BEM method, motivated by some previous work [10, 30, 31], using normal and tangential forces predetermined on the blade, FN and FT obtained from experiments or CFD calculations to calculate the local induction factor, as well as effective local angles of attack and lift and drag forces for each section of the blade (figure 14). The inverse algorithm BEM based on the calculated pressure distributions (3-D calculations done previously) is summarized below:

$$F_{N,i} = \oint \vec{p}.\vec{e}_n dl \qquad (4)$$

And

$$F_{T,i} = \oint \vec{p}.\vec{e}_t dl \qquad (5)$$

1- Initialization of the axial and tangential factors, typically:

$$a = \acute{a} = 0 \qquad (6)$$

Compute the effective inflow angle as fallow:

$$\phi_i = tan^{-1}\left[\frac{(1-a_i)U_\infty}{(1+\acute{a}_i)r\omega}\right] \qquad (7)$$

2- Compute the new values of axial and tangential factors:

$$a_{new,i} = \frac{1}{\frac{8\pi r f sin^2\phi_i}{cBC_{N,i}}+1} \qquad (8)$$

And

$$\acute{a}_{new,i} = \frac{1}{\frac{8\pi r f sin\phi_i cos\phi_i}{cBC_{T,i}}-1} \qquad (9)$$

3- If the difference between the new values of $[a, \acute{a}]$ and $[a_{new}, \acute{a}_{new}]$ is more than certain tolerance, go to step 2. Else, continue.

4- Compute C_l, C_d and the effective angle of attack as :

$$C_{l,i} = C_{N,i} cos\phi_i + C_{T,i} sin\phi_i \qquad (10)$$

$$C_{d,i} = C_{N,i} sin\phi_i - C_{T,i} cos\phi_i \qquad (11)$$

And

$$\alpha_i = \phi_i - \theta_i \qquad (12)$$
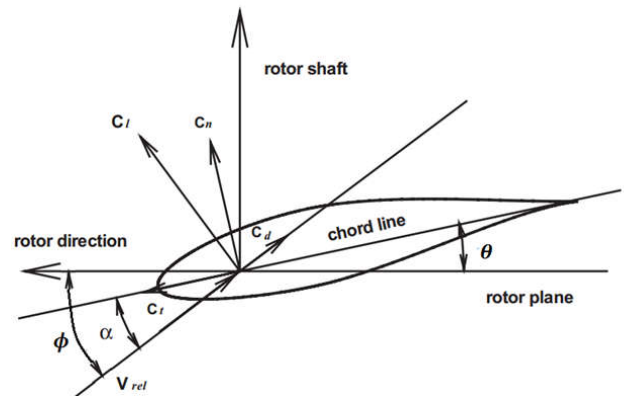
Where θ_i is the pitch angle.

Figure 14.Cross-sectional airfoil element.

In this part, the inverse BEM method was used to determine the angle of attack of the 3-D flow over the NREL Phase II rotor. The Navier-Stokes calculations were made previously for wind speeds of 4, 5, 6, 7.2, 8, 12.85, 16.3 and 19.18 m.s^{-1} with ANSYS FLUENT software. A comparison was made between the results obtained using the method mentioned above and the experimental test data that has been achieved in the wind tunnel of Colorado State University (CSU) [32] and Ohio State University (OSU) [33], and the experimental data from NREL Phase II [32].

Lift and drag coefficient for different radial positions r/R = 0.3, 0.47, 0.63, 0.80 are shown in figures 15 and 16. We can see that the values of drag coefficient show good agreement with those of the experience for all sections of the blade, especially for the sections r/R = 0.63, 0.8. However, the values of the lift coefficient are in reasonable agreement for small values of AoA and begin to deviate from the experimental data when the angle of attack increases.
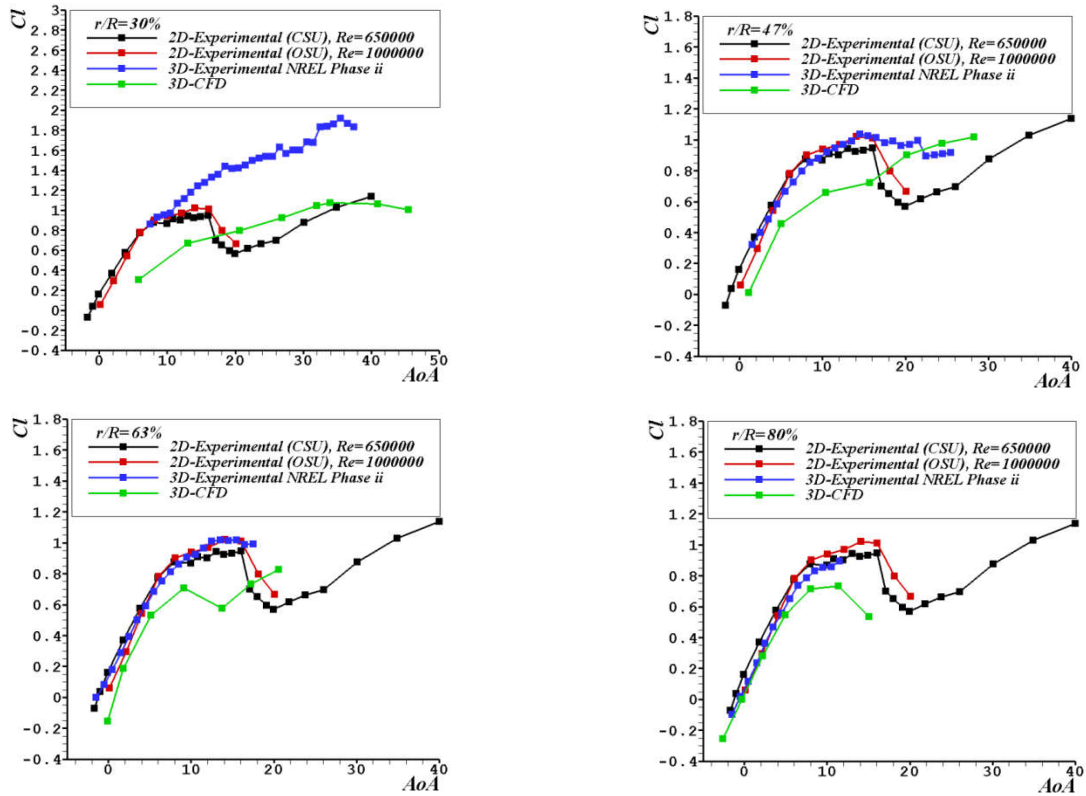
Figure 15. A comparison between lift coefficient as predicted by the inverse BEM method and CFD data at r/R: 0.3, 0.47, 0.63 and 0.8. The 2-D data is taken from wind tunnel experimental results at Re=0.65 x 106 [32], and Re = 1 x 10^6 [33] and the experimental data from NREL [32].
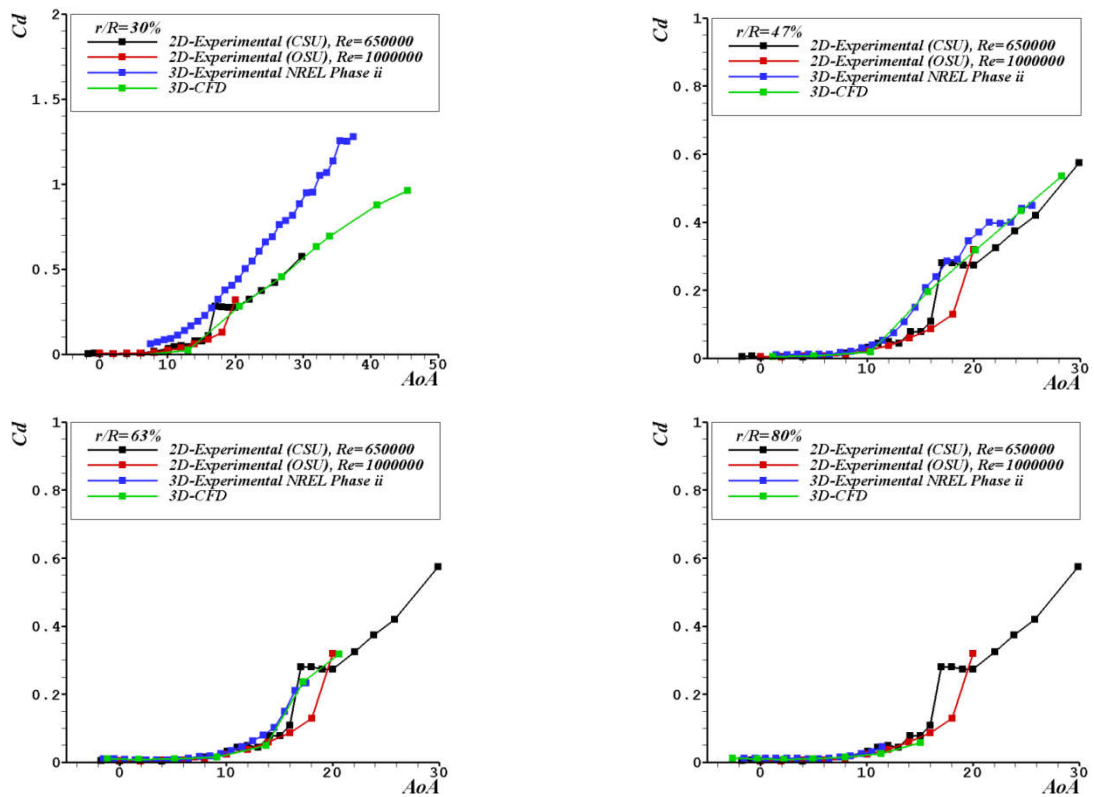

Figure 16. A comparison between drag coefficient as predicted by the inverse BEM method and CFD data at r/R: 0.3, 0.47, 0.63 and 0.8. The 2-D data is taken from wind tunnel experimental results at Re=0.65 x 10^6 [32], and Re = 1 x 106 [33] and the experimental data from NREL [32].

At r/R = 0.30, we see that there is a considerable deviation of the lift coefficient with respect to 2-D experimental data, that disagreement due to the 3-D effect present in the boundary layer of a rotating blade . At the same section (30%), by comparing with experimental data from NREL we observed that they have almost the same trend.

While the general trend is similar for all sections of the scale, large deviation exists between the 2-D and 3-D case. The determination of the effective angle of attack experimentally or numerically is a difficult task and it needs to be done to better determine the angles of attack of the 3-D flow with a rotary blade.

IV. Conclusion

The aim of the current works is the numerical study of HAWT rotor NREL Phase II; the validation of the computed results with experimental data has been done. The results were restricting to pressure and pressure distribution on the blade, generated torque and a general overview of the flow field around the rotor.

Firstly, the numerical pressure distribution is presented and compared with experimental results at 30, 47, 63 and 80% spanwise locations for wind speed 7.2, 12.9 and 19.18 m.s^{-1}. When the flow is completely attached and no separation occurs, the computed pressure distribution at all sections of the blade is in good agreement with the experimental data except up to 30% span. The differences increase with wind speed especially on the suction side of the blade as stronger vortices form close to the root which explains these discrepancies.

Secondly, the computed torque has a better agreement with strain gages measurement than with the generator measurement at wind speed 7.2 m.s^{-1}, while at 10.56 m.s^{-1} the trend is reversed. The CFD values of the power coefficient are found to be in good agreement with those obtained using the BEM method and measured ones for the tested undisturbed wind speed. The maximum computed value of the power coefficient is only about 0.15, achieved at wind speed of 10.56 m.s^{-1} and tip speed ratio 3.59. The power values show considerable differences at higher wind speeds and for predicting the maximum value. For deep stall conditions, the inability of the RANS model to predict aerodynamic loads is well documented. Then, the invers method BEM was used to determine the angle of attack of the 3-D flow over the NREL Phase II rotor.

The general trend of lift and drag coefficients are similar for all sections particularly in the outer part of the blade. However the determination of the effective angle of attack is still a difficult task and it needs to be improved to predict the 3-D flow of a rotating blade.

Finally, the study confirms that RANS simulations are capable of solving with a fair accuracy the different aspects involved in HAWT flow field, thus this confirms that nowadays CFD simulations can be the most important tool for analysis and design of wind turbine rotors.

References

[1] Sorensen J.N. and Shen W.Z. Numerical modeling of wind turbine wakes. Journal of Fluid Engineering, 2002, 124, pp. 393–9.

[2] E. Hau, Wind turbines. Springer: Berlin, 2000.

[3] Carlo Enrico Carcangiu. CFD-RANS Study of Horizontal Axis Wind Turbine.Thesis for the degree of doctor of philosophy, Gagliari.2008.

[4] F.J. Simoes and J.M.R. Graham, A free vortex model of the wake of a horizontal axis wind turbine, 12th British Wind Energy Association Conference, 1990, pp. 161-165.

[5] L. Terrinonii, P. Signoretti, D. Iatauro, C. Romeo, A. Federici. Performance calculation for a vertical axis wind turbine with variable blade pitch, International Journal of Heat and Technology, 2010, 28(2), pp. 147-153

[6] NatalinoMandas.Numerical Prediction of Horizontal Wind Turbine flow. European Wind Energy Conference and Exhibition 2006

[7] A. Le Pape, J. Lecanu. 3D Navier-Stokes computations of a stall-regulated wind turbine. EWEA Delft (Pays-Bas), 19-21 avril 2004.

[8] Gupta, A, Prediction of aerodynamic forces on wind turbine blades using computational fluid dynamics, Master Thesis, Applied Science in Industrial Systems Engineering, University of Regina, 2007.

[9] Monier Ali Elfarra, Horizontal Axis Wind Turbine Rotor Blade: Winglet & Twist Aerodynamic Design & Optimization Using CFD, PhD thesis, in Aerospace Engineering, Medal East technical University, 2011.

[10] H Snel. R. Houwink, J. Bosschers, W.J. Piers, G.J.W. van Bussel and A .Bruining, Sectional prediction of 3D effects for stalled flow on rotating blades and comparison with measurements, In Proceedings of EWEC 93:Lübeck-Travemunde, 1993, pp. 395–9.

[11] H. Himmelskamp, Profile investigation on a rotating airscrew, These doctorat, Göttingen University: PhD Dissertation, 1945.

[12] G. Ronsten, Static pressure measurements on a rotating and non-rotating 2.375m wind turbine bladecomparison with 2D calculations, Journal of Wind Engineering and Industrial Aerodynamics, 1992, 39(1–3), pp. 105–18.

[13] J.L. Tangler and J.D Kocurek, Wind turbine post-stall airfoil performance characteristics guidelines for blade-element momentum methods , In Proc.of 43rd AIAA Aerospace Sciences Meeting and Exhibit, 2005, volume 591, pp. 1–10.

[14] W.R. Sears, Potential flow around a rotating cylindrical blade, Journal Aeronautical Sciences: Readers' Forum, 1950, 17(3):183.

[15] L.E. Fogarty and W.R. Sears, Potential flow around a rotating, advancing cylinder blade, Journal Aeronautical Sciences: Readers Forum, 1950, 17(9):599.

[16] L.E. Fogarty, The laminar boundary layer on a rotating blade, Journal Aeronautical Sciences: Readers' Forum, 1951, 18(4):247

[17] Banks W.H.H. and Gadd G.E. Delaying effects of rotation on laminar separation, American Institute of Aeronautics and Astronautics Journal, 1963, 1(4):941–2.

[18] W.J. McCroskey and H.A. Dwyer, Methods of analyzing propeller and rotor boundary layers with cross flows, Technical Report SP–228, NASA, 1969. pp. 473–514.

[19] J.N Sorensen, Prediction of the three-dimensional stall on wind turbineblade using three-level, viscous-inviscid interaction model, In Proceedings of EWEC 86: Rome, 1986, pp. 429–35.

[20] Z. Du and M.S. Selig The effect of rotation on the boundary layer of a Wind turbine blade, Renewable Energy, 2000, 20, pp. 167–81.

[21] Hu D. Hua O. and Du Z. A. study on stall-delay for horizontal axis wind turbine, Renewable Energy, 2006, 31, pp.821–36.

[22] J.G. Schepers, A.J. Brand, A. Bruining, J.M.R. Graham, M.M. Hand, D.G. Infield, H.A. Madsen, R.J.H. Paynter and D.A. Simms, Final report of IEA Annex XIV: field rotor aerodynamics, ECNC- 97-027, Energy Research Center of the Netherlands, 1997.

[23] D. Simms, S. Schreck, M. Hand and L. Fingersh, NREL Unsteady Aerodynamics Experiment in the NASA-Ames Wind Tunnel: A Comparison of Predictions to Measurements, National Renewable Energy Laboratory, NREL/TP-500-29494, 2001.

[24] ANSYS Inc, Ansys fluent theory guide, November 2010.

[25] Riyadh Belamadi, Abdelouheb Djemili, Adrian Ilinca, Ramzi Mdouki., Aerodynamic performance analysis of slotted airfoils for application to wind turbine blades, Journal of Wind Engineering and Industrial Aerodynamics, 2016, 151,2016, pp. 79–99.

[26] Chalothorn Thumthae, Tawit Chitsomboon, Optimal angle of attack for untwisted blade wind turbine' Renewable Energy, 2009, 34, pp. 1279-1284.

[27] Earl P.N. Duque .Numerical Predictions of Wind Turbine Power and Aerodynamic Loads for the NREL Phase II Combined Experiment Rotor, American Institute of Aeronautics and Astronautics journal, 2000-0038.

[28] Ozlem Ceyhan. Aerodynamic design and optimization of horizontal axis wind turbines by using BEM theory and genetic algorithm, master thesis of graduate school of natural and applied sciences of Middle East technical university, 2008.

[29] Jang-Oh MO and Young-Ho LEE, CFD Investigation on the aerodynamic characteristics of a small-sized wind turbine of NREL PHASE VI operating with a stall-regulated method, Journal of Mechanical Science and Technology, 2012, 26-1, pp. 81-92.

[30] C Lindenburg, Investigation into rotor blade aerodynamics: Analysis of the stationary measurements on the UAE phase-VI rotor in the NASA-Ames wind tunnel Tech, Rep. ECN-C–03-025 ECN, The Netherlands, 2003.

[31] S Guntur, C Bak, N Sorensen, Analysis of 3D Stall Models for Wind Turbine Blades Using Data from the MEXICO Experiment, The 13th International Conference on Wind Engineering, Amsterdam, the Netherlands, 2011.

[32] C.P. Butterfield, W.P. Musial, G.N. Scott, D.A. Simms, NREL Combined Experimental Final Report-Phase II, NREL/TP-442-4807, 1992.

[33] R.R Ramsey, M.J Hoffman, G.M Gregorek, Effects of Grit Roughness and Pitch Oscillations on the S809 Airfoil, NREL TP-442-7817, December 1995.